Article

Role of Fluorine in Chemomechanics of Cation-Disordered Rocksalt Cathodes

Dongchang Chen,[#] Jin Zhang,[#] Zhisen Jiang, Chenxi Wei, Jordan Burns, Linze Li, Chongmin Wang, Kristin Persson, Yijin Liu,* and Guoying Chen*

Cite This: https://doi.org/10.1021/acs.chemmater.1c02118

Read Online

ACCESS | Metrics & More | Article Recommendations | Supporting Information

ABSTRACT: The role of nanoscale chemomechanical behavior in the macroscopic performance of functional materials is well recognized. For lithium-ion battery cathodes, tremendous effort has been devoted to the development of new chemistry and structure, yet fundamental understanding of the correlation between redox processes and mechanical properties of the novel materials lags behind. In the present study, we prepare large discrete single grains of Li-excess cation-disordered rocksalts (DRX) and investigate their chemomechanical behavior at the particle level, using nanoresolution X-ray and electron-based spectro-imaging and chemical mapping techniques. While irregular cracking upon lithium extraction leads to the eventual breakdown of the baseline DRX oxide ($Li_{1.2}Ti_{0.4}Mn_{0.4}O_2$) particles at a high delithiation state, the fluorinated-DRX ($Li_{1.3}Ti_{0.3}Mn_{0.4}O_{1.7}F_{0.3}$) clearly displays aligned cracking along the <001> direction. The resulting periodicity in the cracking pattern enables the particles to retain their integrity and, consequently, improved electrochemical stability. Density functional theory (DFT) calculations showed that fluorination leads to increased concentration of Li^+ on the (001) planes and preferential Li movements along the <001>-family directions, revealing the underlying mechanism for directional cracking. Our study demonstrates the unique role of fluorine in modulating nanoscale chemomechanics, which in turn influences the evolution of charge and strain heterogeneity at the particle level. These insights provide important design guidelines in further improving DRX cathode materials.

Fluorination in DRX leads to directional cracking
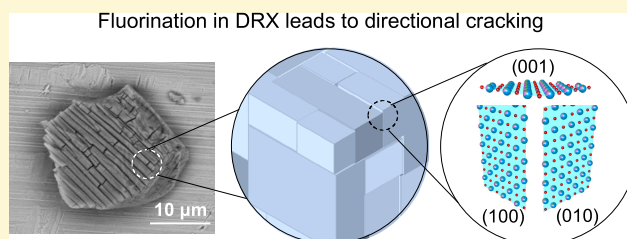
1. INTRODUCTION

The development of lithium-ion battery (LIB) electrode materials with high-energy densities is of vital importance for both fundamental and applied energy sciences.[1−3] In the engineering perspective, whether a new electrode material can be eventually implemented into devices strongly depends on its chemomechanical behavior.[4−10] Chemomechanics reflects the fundamental relationship between chemical changes and mechanical responses in materials and vice versa.[11] The topic covers a wide range of subjects in chemistry, materials sciences, and mechanical engineering.[11−13] In battery materials, chemomechanics is often manifested by the changes in mechanical properties, such as strain accumulation and release that lead to cracking, deformation, or morphological changes of active particles, upon the progression of chemical redox reactions.[14,15] It determines materials utilization and stability in a broad range of time and length scales. At the nanoscale, for example, mechanical breakdown at the particle level hinders the direct solid-state ionic and electronic conduction pathways within the particle.[4−6,16−18] The infiltration of liquid electrolyte through the cracks,[17] on the other hand, creates a new solid-electrolyte interface that could improve the ionic conduction, although in the long run, the increased surface area may lead to enhanced side reactions and, consequently,

more degradation. At the macroscale, detachment of active materials from the conductive matrix directly impedes the electronic conduction from current collectors.[7] In recent years, efforts have been directed toward the understanding of chemomechanical behavior in state-of-the-art cathode materials like lithium nickel manganese cobalt (NMC) oxides[16,19−21] as well as anode materials like graphite and silicon.[22] Critical factors influencing the crystallographic direction of cracks and cracking propagation rate, as well as the correlation between intergrain and intragrain cracks, were investigated.[4,5,17,18] This knowledge has enabled electrochemical performance enhancement *via* the tuning of chemomechanical properties.[4,5,8,15,19]

Recently, Li-excess cation-disordered rocksalt (DRX) compounds, with a simple NiO-like crystal structure and random cation distribution in the long range, emerged as a new class of Co-free high-energy LIB cathode materials.[23−27] While significant performance degradation was reported on oxide
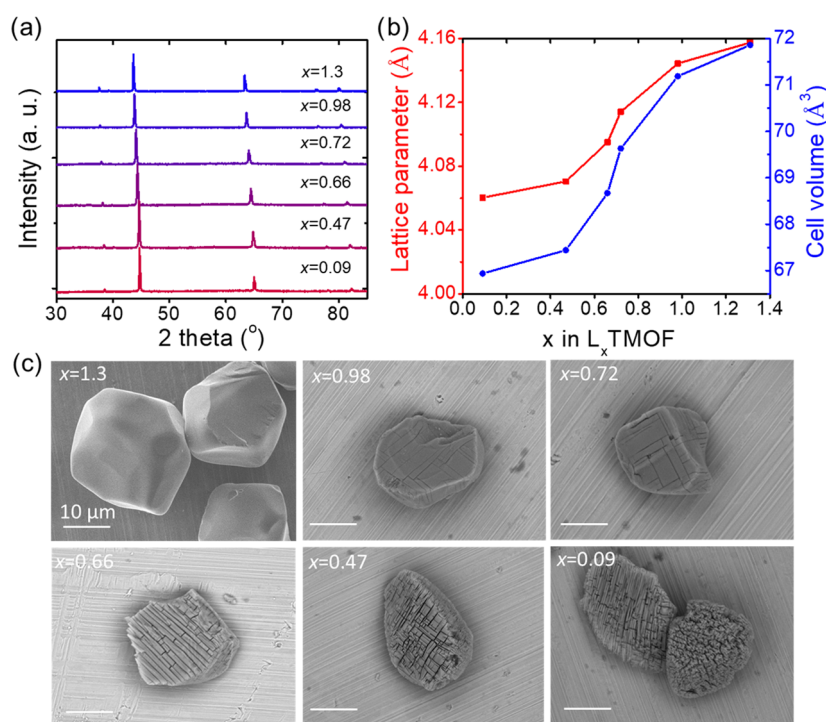
Figure 1. (a) XRD patterns collected on L_xTMOF samples, (b) relationship between lattice parameter, cell volume, and Li content in L_xTMOF, and (c) SEM images of L_xTMOF particles. x values as indicated. All scale bars are 10 μm.

cathodes, fluorine substitution into the anionic sublattice has shown promises as an effective strategy in improving cycling stability.[25,28−32] So far, the chemomechanical behavior and its impact on the electrochemical performance of DRX cathodes have not been investigated. It is also unclear whether fluorine substitution has an impact on DRX chemomechanical behavior and the performance improvement in the fluorinated-DRX (F-DRX) is correlated with the changes in chemomechanics.

As chemomechanical coupling is typically far from the thermodynamic equilibrium state, the process can be challenging to quantify both theoretically and experimentally. In this study, we prepared well-formed DRX single grains and investigated particle-level chemomechanical evolution in one of the F-DRX compound, $Li_{1.3}Ti_{0.3}Mn_{0.4}O_{1.6}F_{0.3}$ (LTMOF). The behavior was further compared to that of the baseline DRX oxide, $Li_{1.2}Ti_{0.4}Mn_{0.4}O_2$ (LTMO). Delithiation led to directional cracking in LTMOF, with the correlation between the periodicity in particle cracking pattern and the hetero-geneity in Mn valence distribution revealed for the first time *via* systematic X-ray spectro-imaging and chemical mapping. Transmission electron microscopy (TEM)/selected area electron diffraction (SAED) analysis further identifies <001> as cracking directions. In contrast, lithium removal from the baseline LTMO induced cracking in random directions on the particle, which led to its eventual breakdown at high delithiated states. We report that the unique chemomechanical behavior of DRX oxyfluoride largely contributes to its enhanced cathode performance.

2. RESULTS AND DISCUSSION

2.1. Synthesis and Properties. $Li_{1.2}Ti_{0.4}Mn_{0.4}O_2$ baseline was synthesized using a molten-salt method described in our previous publication.[33] The sample consists of discrete spherical particles with an average size of about 5 μm, as shown in the scanning electron microscopy (SEM) image in

Figure S1a. Rietveld refinement of the X-ray diffraction (XRD) pattern (Figure S1b) confirms NiO-like rocksalt structure with a lattice parameter of 4.1571 Å. Single-grain $Li_{1.3}Ti_{0.3}Mn_{0.4}O_{1.7}F_{0.3}$ sample was synthesized *via* a solid-state self-flux method. LiF (m.p. = 848 °C) was used as a fluorine precursor as well as a molten-salt flux to facilitate crystal nucleation and growth. This leads to the formation of much larger particles with an average particle size of about 20 μm (Figure S2a). Elemental mapping using energy-dispersive X-ray (EDX) analysis shows uniform distribution of Ti, Mn, O, and F at the particle level. Figure S2b,c shows Rietveld refinement of X-ray diffraction (XRD) and neutron diffraction patterns, respectively. The results confirm LTMOF rocksalt phase with a slightly larger lattice parameter of 4.1577 Å.

The phase purity of the synthesized LTMO and LTMOF samples was further confirmed by synchrotron wide-angle X-ray scattering (WAXS) analysis. The obtained XRD patterns (Figure S3) clearly show single-phase rocksalt. Due to the large particle size, crystalline domain size estimation from Rietveld refinement was unsuccessful, even after incorporating an instrumental resolution function file to exclude instrumental factors on line width contribution.

Figure S4 compares the electrochemical performance of LTMO and LTMOF half-cells. The initial discharge capacities were ∼200 and 240 mAh/g for LTMO and LTMOF, respectively (Figure S4a,b). After 50 cycles, capacity and voltage retentions of ∼70 and 80% were achieved on LTMOF, respectively, while that of LTMO were at lower values of ∼ 60 and 70% (Figure S4c−f). In a recent study, we carefully investigated the role of F in DRX behavior other than chemomechanical properties.[34] Through careful monitoring of chemical, structural, and redox evolution in three DRX compounds, LTMO, LTMOF, and $Li_{1.2}Ti_{0.2}Mn_{0.6}O_{1.8}F_{0.2}$, we showed that DRX cycling induces Mn reduction and degradation of its local coordination environment. F
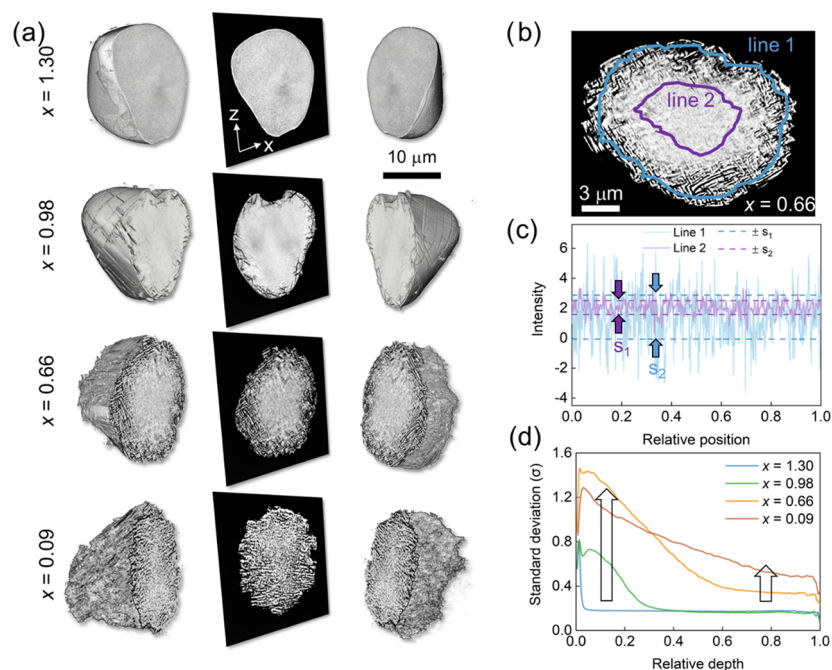
Figure 2. (a) Evolution of 3D tomography rendering of L_xTMOF particles with a virtual central slice, (b) two outlined contours (inner side and outer side) of the central slice of a $L_{0.66}$TMOF particle, (c) standard deviation of the X-ray absorption intensity for the two contours shown in (b), and (d) averaged standard deviation as a function of relative depth (0 for the surface of the particle and 1 for the center of particle) on L_xTMOF particles.

substitution into the oxygen sublattice accompanied by the reduced Li/Mn ratio greatly mitigates this degradation process, demonstrating the positive role of F in the redox processes.

To investigate the relationship between the redox processes and mechanical properties, chemical oxidation[35−37] was used to gradually remove Li and synthesize samples with varying degrees of delithiation. The method allows for the use of as-synthesized DRX large particles for single-particle-based microscopic/spectroscopic analysis. To electrochemically charge and discharge DRX cathodes, samples are often subject to extensive ball milling with a carbon additive prior to electrode making.[23,24,38] This process reduces DRX particle size as well as the quality of the sample needed for imaging analysis. The presence of carbon and binder in the conventional composite electrodes further introduces ambiguity and artifacts in microscopic studies. To this end, a series of L_xTMO (x = 1.2, 0.87, 0.41, and 0.02) samples were prepared by reacting pristine LTMO particles with varying amounts of nitronium tetrafluoroborate (NO_2BF_4, $E_{NO2^+/NO2} \approx 5.1$ V vs Li/Li$^+$) oxidant dissolved in acetonitrile solvent. Similarly, a series of L_xTMOF (x = 1.3, 0.98, 0.72, 0.66, 0.47, and 0.09) samples were prepared by mixing pristine LTMOF particles with varying amounts of NO_2BF_4 solution in acetonitrile. In both cases, the amount of remaining lithium in the oxidized sample, controlled by the mole ratio between the DRX and NO_2BF_4, was determined by inductively coupled plasma (ICP) analysis. Figure S5a shows the powder XRD patterns collected on the L_xTMO series. Upon Li extraction, diffraction peaks systematically shift toward higher angles, indicating lattice contraction. Peak broadening and an overall reduction in peak intensity were also observed, although the rocksalt crystal structure remained throughout the series. Further analysis by Rietveld refinement of XRD patterns was performed (Figure S6), and the results reveal the evolution of lattice parameter and unit cell volume as a function of Li content (Figure S5b).

The lattice parameters for the two end members in the series, x = 1.2 and 0.02, were 4.1571 and 4.0703 Å, respectively. The cell volume decreased from 71.84 to 67.44 Å^3, corresponding to a total volume change of about 6.1%. The refinement parameters are listed in Table S1.

For comparison, the XRD patterns collected on the L_xTMOF series are shown in Figure 1a. Upon Li extraction, the rocksalt crystal structure remains in all samples, but the diffraction peaks systematically shift toward higher angles, corresponding to lattice contraction. Unlike the case with the baseline and other DRX oxides,[26,37] peak broadening was not observed even after removing a substantial amount of Li. This is clearly shown in Figure S7a where the (220) diffraction peak of the XRD profiles collected on the pristine LTMO and LTMOF along with delithiated $L_{0.02}$TMO and $L_{0.09}$TMOF are compared. The well-preserved peak widths indicate that the crystallinity of LTMOF largely remains after delithiation. Additional analysis using the Williamson-Hall method (details can be found in Supplementary Note 1.1) suggests that the peak broadening in the delithiated $L_{0.02}$TMO is largely due to reduced particle size, whereas in $L_{0.09}$TMOF, the minor peak broadening is a result of particle-level strain (Figure S7b). We note that similar behavior was also observed on electrochemically charged LTMO and LTMOF particles. Figure S8a,b compares XRD patterns collected on LTMO and LTMOF electrodes at the pristine state and after the first charge. Peak broadening in charged LTMO is much more significant than that of LTMOF. Williamson-Hall analysis (Figure S8c) shows that while the slopes of the charged LTMO and LTMOF are similar, the intercept of charged LTMO is much higher, indicating that the observed peak broadening in LTMO is largely due to reduced particle size upon charging, which is consistent with the observation from chemically delithiated samples.
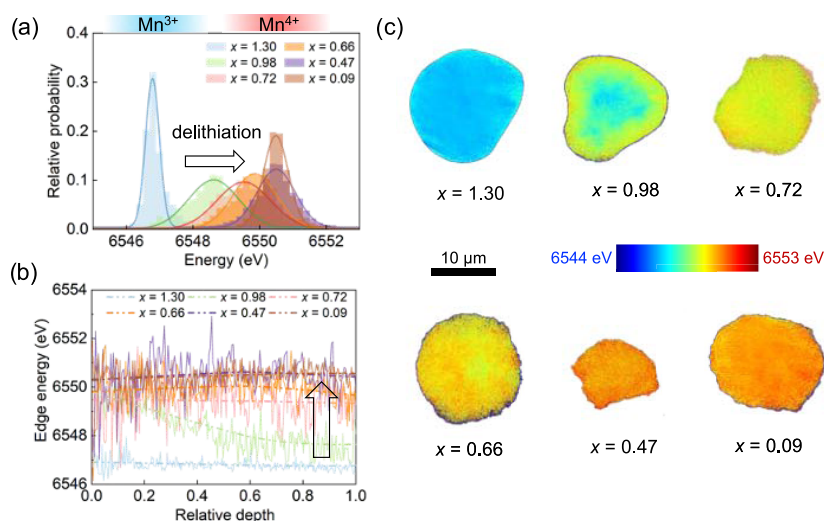
Figure 3. (a) Evolution of K-edge energy distribution as a function of the lithium content x, (b) variation of edge energy as a function of relative depth on L_xTMOF particles, and (c) 2D Mn K-edge energy distribution mapping of L_xTMOF with different x values.

The evolution of lattice parameter and unit cell volume as a function of Li content in L_xTMOF was also obtained (Figure 1b) by Rietveld refinement of XRD patterns (Figure S9). The refinement parameters are also listed in Table S2. The plot adopts a near S shape, suggesting that lattice contraction is relatively slower at an either low or high degree of delithiation. The lattice parameters for the two end members in the series, x = 1.3 and 0.09, were 4.1577 and 4.0603 Å, respectively. The cell volume decreased from 71.87 to 66.94 Å^3, corresponding to a total volume change of about 6.9%, which is slightly higher than that in LTMO baseline.

Figure 1c shows the SEM images collected on the L_xTMOF series, which displays morphological evolution as a function of lithium content. At the pristine state, particles show a smooth but well-faceted surface. Upon delithiation, parallel cracks developed along a single direction of the particle, with the density of the cracks increasing along with the degree of delithiation. At high delithiation states, cracks along the perpendicular direction of the initial cracks also developed. This unique cracking behavior is largely absent in the baseline LTMO sample. As shown in Figure S10, particle cracking due to delithiation is mostly in random directions. As a result, L_xTMO particles broke into small pieces at the high delithiation state of x = 0.02.

We note that due to the high chemical potential of NO_2BF_4, the chemical delithiation process is equivalent to charging DRX at a constant high voltage. Under these conditions, some TM dissolution may occur.[35,39−41] However, we believe that its contribution toward particle cracking is minor, based on our previous experience on the chemical delithiation of similar cathode materials.

2.2. Spectro-Imaging and Chemical Mapping. To further understand the cracking behavior and chemomechanical coupling in DRX, we performed systematic spectro-imaging and chemical mapping using both X-ray and electron-based techniques. Transmission X-ray microscopy (TXM) is a powerful tool capable of monitoring morphological changes as well as resolving chemical and compositional distributions at a nanoscale resolution.[6,7,17,18] By integrating transmission X-ray images acquired in systematically tuned viewing angles, computed tomography with a spatial resolution ~30 nm (nano CT) can be reconstructed to reveal the fine internal

particle structures, e.g., inclusions, voids, and cracks, in a noninvasive manner. Figure 2a shows the three-dimensional (3D) rendering of L_xTMOF particles as a function of Li content. The virtual slices through the center of the reconstructed particles are also shown to highlight the inward propagation of the cracks. The pristine particle demonstrates a smooth cross-section, consistent with the surface observation made on SEM. In tomographic scans, twining domains in a single crystalline particle are easily discerned by the contrast in the transmission image, caused by the asynchronous activation of the Bragg diffraction. This is because when a domain or grain satisfies the Bragg condition in a certain angle, it diffracts more photons away from the transmission detector and leaves an enhanced contrast in the transmission image. After thoroughly varying projection angles and carefully reviewing all of the reconstructed TXM images, LTMOF particles were found to be entirely featureless absence of contrast at the particle level, confirming the single crystalline nature of the pristine sample.

Upon delithiation, the number of cracks is positively correlated with the degree of delithiation and internal cracks also appear to be well aligned. At a low stage of delithiation (e.g., x = 0.98), cracks mainly occur in the near-surface regions of the particle and the core region remains intact. With further delithiation (e.g., x = 0.66 and 0.47), the cracks extend into the core region of the particle and the density gradually increases.

To further evaluate the depth-dependent particle cracking pattern, we quantify the intensity variation in the tomography contours at different depths. Figure 2b outlines two contours at different depths of a $L_{0.66}$TMOF particle. The standard deviation quantifies the intensity variation over the selected contour line and is an effective measurement of the degree of particle cracking at the corresponding location. As shown in Figure 2c, Line 1 (the outer part of the particle) demonstrates a significantly higher standard deviation than line 2 (the inner part of the particle). The averaged standard deviation as a function of relative depth (0 for the surface of the particle and 1 for the center of the particle) collected on the examined L_xTMOF particles is shown in Figure 2d, which was obtained by quantifying the particle's entire volume pixel by pixel in 3D. The results suggest that cracking initiates at the near-surface region and then propagates inward as more lithium cations are
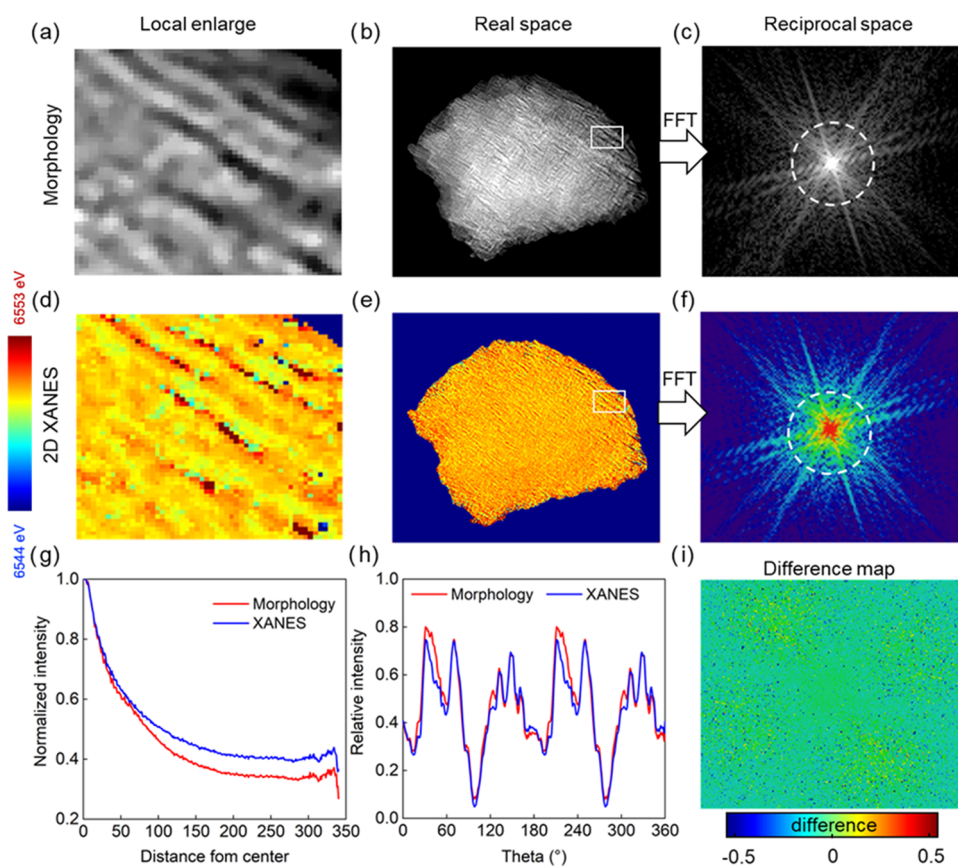
Figure 4. X-ray absorption images and Mn K-edge energy maps collected on a $L_{0.47}$TMOF particle: (a, d) locally enlarged, (b, e) full-field real-space data, and (c, f) reciprocal-space data obtained from 2D FFT of real-space data. (a−c) X-ray absorption images and (d−f) Mn K-edge energy maps. (g) Fourier power spectrum of morphology and XANES map shown in (c) and (f). (h) Intensity variation over the two circles on 2D FFT maps in panels (c) and (f). (i) Difference map of 2D FFT maps.

removed from the particle. The observed depth-dependent cracking behavior also hints at an outward lithium diffusion pattern, which may result in charge and crack heterogeneities at the particle level.

The evolution of Mn oxidation state as a function of lithium content in the sample was also investigated. During TXM measurements, 2D spatially resolved X-ray near-edge absorption spectroscopy (XANES) can be performed by analyzing X-ray transmission images with systematically tuned excitation energy, which enables direct visualization of a given TM's chemical state variation at nanoscale resolution (∼30 nm). Figure 3a shows Mn K-edge energy distribution in L_xTMOF at the indicated lithium content x. The edge energy of each pixel, determined based on the absorption intensity of 0.5 in the normalized spectrum of each pixel (without pixel binning), was used to quantify the local oxidation state of Mn. A note on data processing can be found in the Supporting Information (Supplementary Note 1.2 and Figure S15). At the pristine state, the range matches well with that of Mn^{3+}. Upon initial Li removal, a gradual increase in the overall Mn K-edge energy was observed, indicating Mn oxidation. These changes were still observed on the samples with a lithium content between 0.66 and 0.47, but no further Mn oxidation was found after x reaches 0.47, where the edge energy distribution falls into the range of Mn^{4+} (Figure 3a). We note that along with the overall increase in Mn oxidation state, the distribution in Mn K-edge energy also became broader. Figure 3b shows the variation of the edge energy as a function of relative depth from the surface

to the center of the particle (0 for the surface and 1 for the center of the particle). In general, the near-surface region subjects to more variation than the core region of the particle. Such location-dependent variation is likely the cause for the observed broad distribution in edge energy shown in Figure 3b. The resulting 2D Mn chemical maps of L_xTMOF particles at different stages of delithiation are also shown in Figure 3c. To ensure statistical relevance of the experiment results, multiple particles were evaluated (details can be found in the Supporting Information, Supplementary Note 1.3, Figure S16). At the intermediate states ($x = 0.98, 0.72$, and 0.66), the distribution of Mn oxidation state at the particle level is largely heterogeneous. Oxidation appears to initiate on the surface at the low delithiation state, which then progresses toward the core of the particle upon further delithiation. The uniformity in Mn oxidation state improves after the Li content reaching 0.47.

Our previous studies showed that during constant current charging to an upper cutoff voltage of 4.8 V, Mn cationic oxidation occurs at a lower voltage followed by the oxidation of oxygen anions at higher voltage.[26,42] As the Mn content in $Li_{1.3}Ti_{0.3}Mn_{0.4}O_{1.7}F_{0.3}$ is 0.4 per formula unit, charge compensation for Mn^{3+} to Mn^{4+} redox corresponds to the removal of 0.4 Li, or $x = 0.9$ in the sample. Here, Mn oxidation state change was observed well below $x = 0.9$. The discrepancy is likely due to the delithiation method used. In chemical delithiation with NO_2BF_4, particles are subject to a constant voltage of ∼5.1 V vs Li^+/Li. This may promote some degree of mixed redox processes from both Mn and O, leading to
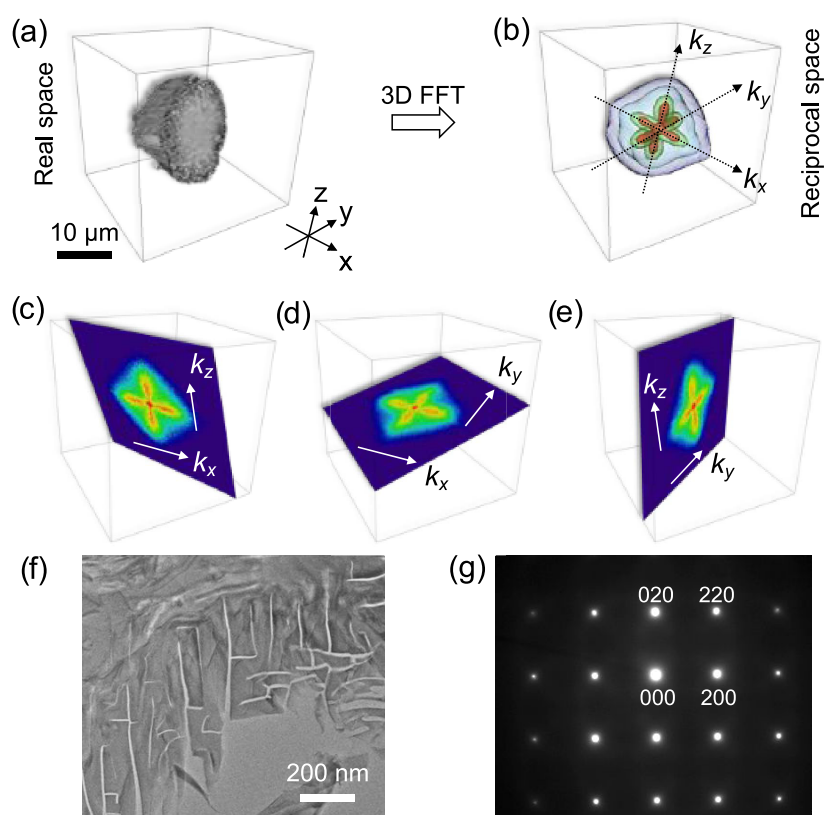
Figure 5. (a) Real-space 3D rendering of a $L_{0.66}$TMOF particle with the virtual central slice, (b) isosurface of 3D rendering of a $L_{0.66}$TMOF particle in the reciprocal space obtained from 3D FFT of the real-space tomography, (c−e) cross-sections of the isosurface on xz, xy, and yz planes, respectively, (f) TEM image of a slice of $L_{0.66}$TMOF fabricated by a focused ion beam (FIB), and (g) SAED pattern of the TEM image shown in (f).

changes in Mn oxidation state at a much higher delithiation state than what was observed in galvanostatic charging.

Similar to the observation in crack density evolution, it is clear that Mn K-edge energy variation is closely correlated with the extent of delithiation. To elucidate the interplay between electrochemical processes and mechanical properties of LTMOF, we closely examined the features present in both morphological and chemical maps. Figure 4b,e compares the 2D X-ray absorption image and XANES map collected on a $L_{0.47}$TMOF particle, respectively. The local enlarged views of the highlighted areas are shown in Figure 4a,d, respectively. Careful visual assessment of the data suggests that spatially, the dark strips in the X-ray absorption image (Figure 4a), which correspond to the aligned cracks along the same direction, match well with the red strips in the 2D XANES map (Figure 4d), indicating higher Mn oxidation state. On the other hand, the brighter regions in the X-ray absorption image correspond well to the yellow regions in the 2D XANES image, indicating a lower Mn oxidation state. The strong correlation is also shown in the gridlike patterns in the full-field view of both X-ray absorption image and Mn oxidation state map (Figure 4b,e), which can be considered as 2D periodic signal distribution in the real space. To further investigate the nature of the periodicity, 2D Fourier Transform (FT) patterns of the real-space X-ray absorption image and the 2D XANES map were obtained (Figure 4c,f), which visualize the data in the reciprocal space. The aligned grids in Figure 4b,e correspond to the spikes in the signals shown in Figure 4c,f, further demonstrating the correlated nature of particle-level chemomechanical interplay in LTMOF.

The Fourier power spectra can be considered as the density of features as a function of the frequency of these features. Figure 4g compares the Fourier power spectra of morphology and XANES map, which are highly consistent. Data from the XANES map shows an enhancement over the high-spatial-frequency regime. This is because the XANES map removes the sample thickness information during the spectrum normalization process, which promotes high-spatial-frequency components in the image and in the power spectrum. The similarity in the angular dependence of FFT patterns was evaluated by plotting the intensity variation over the two highlighted circles on 2D FFT maps (Figure 4c,f). The results show overlapping peaks (Figure 4h), consistent with matching orientations of the real-space features in the two maps (Figure 4b,e). The difference map of 2D FFT maps is also shown in Figure 4i, which appears rather flat with a few "salt-and-pepper" features. Overall, these quantitative analyses further confirm that morphological features and chemical features are strongly correlated.

3D FT analysis that transforms the 3D real-space morphology into reciprocal-space patterns was also performed. Figure 5a shows the real-space 3D rendering of a $L_{0.66}$TMOF particle with the virtual central slice showing the aligned cracks. The 3D visualization of the Fourier space data (Figure 5b) shows the maxima along the three orthogonal directions (i.e., x, y, and z). On each plane of the reciprocal space (i.e., xy, yz, and xz planes), the cross-section of the 3D FT pattern demonstrates evenly spaced orthogonal maxima (Figure 5c−e), suggesting that the cracks are orthogonally distributed with similar spatial frequency in each orientation.
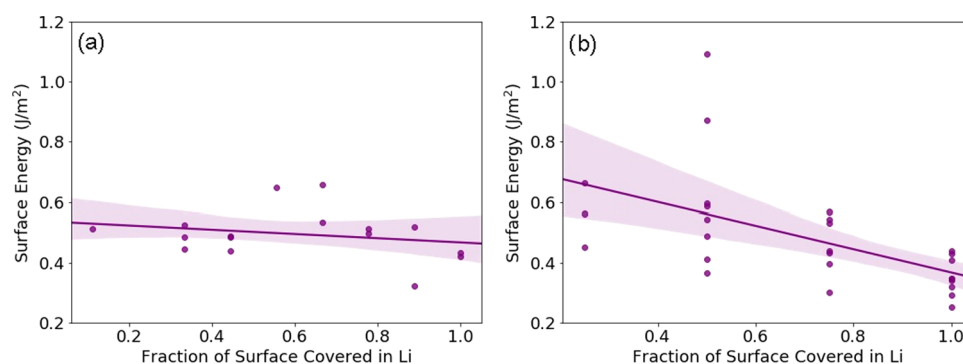
Figure 6. Surface energy as a function of the fraction of the surface covered in Li^+ for (001) facets of (a) LMO and (b) LMOF. The dark purple line indicates the best fit through the data. The purple shaded area shows a 95% confidence interval for the line of best fit found by bootstrapping the data sampling it 1000 times.

The crystallographic orientation of the cracks was further investigated by transmission electron microscopy (TEM) analysis. To prepare for TEM studies, focused ion beam (FIB) was used to slice the particle along the direction of cracking. As shown in Figure 5f, when the image was taken along the zone axis aligned with the cracks, the obtained SAED pattern displays evenly spaced orthogonal diffraction spots (Figure 5g). The results suggest that cracking in LTMOF occurs along the <001> directions. We note that in cation-disordered rocksalt crystal structure, [001, 010] and [100] directions are crystallographically equivalent, all belonging to the <001> family.

Such directional cracking is largely absent in the baseline LTMO. Figure S11 compares the evolution of 2D XANES maps of L_xTMOF and L_xTMO as a function of Li content x. In contrast to L_xTMOF particles which remain intact with increasing delithiation, L_xTMO particles only maintained particle shape at lower oxidation states (i.e., $x > 0.87$). Cracks with random orientations can be seen in these samples. At higher oxidation states, L_xTMO particles disintegrate into smaller pieces. As the size of LTMOF particles is nearly 4x larger than that of LTMO, the role of particle size in chemomechanics was examined. Figure S12a,b shows the SEM images collected on partially delithiated L_xTMOF ($x = 0.66$) particles with a smaller particle size of ~6−8 and 10−15 μm, respectively. All examined particles displayed the directional cracking similar to what was observed on delithiated L_xTMOF particles in the 20 μm size range. Moreover, the size range of 6−8 μm is reasonably close to 5 μm (the size of LTMO). We believe that particle size does not contribute to the observed differences in a significant way.

Due to charge neutrality, fluorine substitution inevitably leads to changes in stoichiometry. To rule out contribution from other factors such as Li/TM ratio in cracking, similar studies were performed on other DRXs with varying Li and TM combinations and stoichiometries. As shown in Figures S13 and S14, delithiated $Li_{1.2}Ti_{0.2}Mn_{0.6}O_{1.8}F_{0.2}$ and $Li_{1.37}Nb_{0.21}Mn_{0.42}O_{1.67}F_{0.33}$ exhibited directional cracking similar to what was observed on LTMOF, suggesting that the observed differences are not related to the changes in the ratio between Li and TM. Directional cracking observed in LTMOF is likely a result of fluorine substitution into the oxygen anionic sublattice.

2.3. Density Functional Theory (DFT) Calculations. In recent years, much progress has been made in understanding the role of fluorine in DRX behavior and electrochemical performance, both in theoretical calculations and experimental studies.[29−31] It was found that fluorination leads to less oxygen release, less impedance rise, and better cycling stability of DRX cathodes. Fluorine substitution also greatly impacts short-range ordering in the cation-disordered structure and, consequently, Li percolation pathways and kinetics.[23]

To understand the unique ability of fluorine in modulating nanoscale chemomechanics in DRX oxyfluorides, density functional theory calculations were performed. Because of the structural complexity of LTMO and LTMOF, two simpler model compounds with the same Mn(III) cation and similar random cation/anion distributions in the cubic $Fm\overline{3}m$ structure, $Li_{1.5}Mn(III)_{1.5}O_3$ (LMO) and $Li_2Mn(III)O_2F$ (LMOF), were chosen to investigate the effect of fluorination. A cluster expansion Monte Carlo method developed by Ouyang et al.[31] was used to construct the disordered structures. Figure S18 shows an example of how symmetric (100)-type surfaces from LMOF were constructed. Different configurations of (001) planes with varying fractions of Li^+ were then systematically surveyed in the calculation. The statistical results showed that for LMO, the variation on (001) surface energy with different Li^+ fractions is insignificant (Figure 6a), whereas on LMOF, Li-enriched (001) surfaces were found to be much more stable than the Li-poor (001) surfaces (Figure 6b). The lowest energy surface found for LMOF was completely covered in Li^+, while the lowest energy surface of LMO was not completely covered in Li^+ and had some fraction of Mn^{3+} (Figure S19).

These results suggest that fluorination strongly correlates with increased concentration of Li^+ on the (001) planes. During charge and discharge, more Li cations move in and out along the <001> crystalline directions. We believe this creates enhanced mechanical stress where dislocations/slip are more likely to occur, resulting in preferential cracking along these directions. As <001>, <010>, and <100> directions are crystallographically equivalent in $Fm\overline{3}m$ crystal structure, the end result is a unique periodic cracking pattern observed on SEM images (Figure 1) and X-ray tomography (Figure 2). The lack of preferential Li movement in the oxide counterpart, on the other hand, led to cracking in random directions.

2.4. Discussion. A significant impact of chemomechanics in the electrochemical behavior of cathode materials has previously been demonstrated.[4−10] The unique role of fluorine in modulating nanoscale chemomechanics can further influence the evolution of charge and strain heterogeneity at the particle level. Figure 7 shows the schematics where the
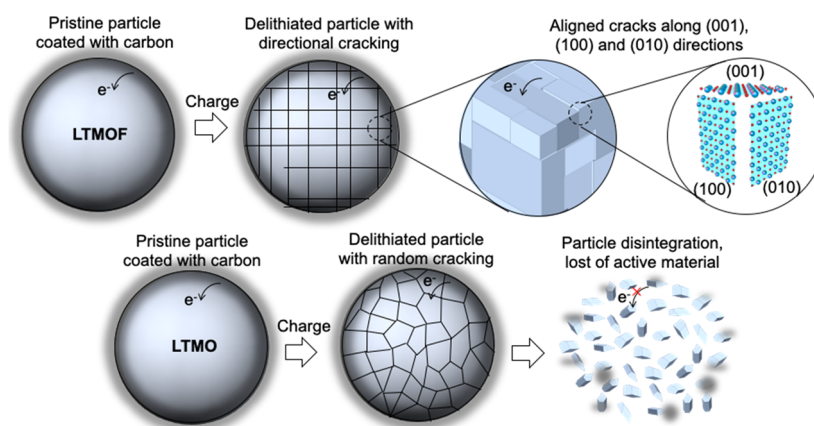
Figure 7. Schematics showing the effect of chemomechanical behavior on the electrochemical performance of DRX oxide and oxyfluoride cathodes.

effects of chemomechanical behavior on electrochemical charge of DRX oxide and oxyfluoride cathodes are compared. For oxyfluoride, cracks develop along the <001> direction upon lithium extraction, simulating "slicing" from the particle surface along particular directions. Since [001, 010] and [100] directions are perpendicular to each other yet equivalent in the rocksalt crystal structure, the particles show a cracking pattern with periodicity while maintaining integrity. This enables sufficient connection for electronic conduction to occur throughout the particle, which is key to electrochemical extraction and insertion of lithium. In contrast, lithium removal leads to the formation of cracks along random directions in DRX oxide cathodes, which makes them more likely to extend into the bulk. Upon deep extraction of lithium, the cracks intersect with each other, causing the particle to disintegrate and fall into small pieces. The net effect is the breakdown of surface carbon coating and loss of electronic connection among the pieces. Since these changes are irreversible, the progressing deterioration in material leads to capacity fade over cycling. The difference in the chemomechanical behavior is consistent with the observed electrochemical performance of DRX oxide and oxyfluoride cathodes (Figure S4), further confirming the importance of an interplay between redox processes and mechanical properties. Although fluorination may also induce other facet-dependent effects, such as redox potentials of Mn redox and O redox, surface O loss, and side reactions with the electrolyte, our study suggests that heterogeneity in Li distribution is the dominating cause for the observed chemomechanical behavior.

3. CONCLUSIONS

In this work, we prepared well-formed single grains of a DRX oxide and oxyfluoride and used them to explore their intrinsic chemomechanical behavior. We showed the unique role of F in modulating the nanoscale evolution of oxyfluoride mechanics, where directional cracking was observed upon delithiation. In contrast, delithiation leads to randomly oriented cracks in the DRX oxide baseline sample. X-ray nanotomography measurements and 2D XANES imaging revealed the correlation between the aligned cracks and the variation in Mn oxidation state. Crystallographic analysis through TEM/SAED further determined <001> directions as the preferential cracking direction in oxyfluoride. DFT calculations of different surface decorations, using bulk compositions obtained from a previous cluster expansion Monte Carlo methodology,[31] revealed that

fluorination leads to increased concentration of Li$^+$ on the (001) planes, which is expected to lead to preferential Li movements along the <001>-family directions. The unique chemomechanical behavior of DRX oxyfluoride enables its enhanced electrochemical cycling stability. The insights obtained in this study provide important design guidelines for the future development of DRX cathode materials.

4. EXPERIMENTAL SECTION

4.1. Synthesis. LTMO was synthesized using a molten-salt method as described in a previously publication.[33] LTMOF was synthesized using a solid-state self-flux method. Li$_2$CO$_3$, TiO$_2$, Mn$_2$O$_3$, and LiF (Sigma-Aldrich) precursors were ball-milled with ethanol at 200 rpm for 18 h in a planetary ball mill (RETSCH PM100). Typically, 10–15 mol % of excess Li$_2$CO$_3$ was added to compensate for potential Li loss during calcination at high temperatures. Excess LiF (typically 15–20 mol %) was also used to serve as both F source and a molten flux for the nucleation and growth of oxyfluoride single grains. The ball-milled mixture was then dried, further ground, and heated at 950 °C for 12 h in an Ar-atmosphere quartz tube furnace, using a ramping rate of 4 °C/min. The salt residues in the calcined product were removed by thoroughly washing with deionized water (LiF solubility in water is 127 mg/100 mL). The obtained final powder was dried overnight at 80 °C in a vacuum oven.

Chemically delithiated L$_x$TMO and L$_x$TMOF samples were prepared by reacting the pristine powder with various amounts of 0.1 M nitronium tetrafluoroborate (NO$_2$BF$_4$, Sigma-Aldrich) in acetonitrile solution in an argon-filled glovebox (O$_2$ < 1 ppm and H$_2$O < 1 ppm). The reaction was carried out at room temperature for 24 h. The resulting reaction mixtures were centrifuged, thoroughly washed with acetonitrile inside the glovebox, and then dried overnight in a vacuum oven. Note that NO$_2$BF$_4$ is a strong oxidant and highly hygroscopic. The oxidation process generates NO$_2$, which is a toxic gas. The reaction between NO$_2$BF$_4$ and water generates HF, which is highly corrosive.

4.2. Characterization. Sample morphology and EDX elemental mapping were carried out using a scanning electron microscope (JEOL JSM-7500F). The phase purity of pristine and delithiated powders was evaluated using a Bruker D2 powder X-ray diffractometer (Cu Kα, 40 kV, 30 mA, with a small amount K$_\beta$ radiation also detected) and synchrotron XRD carried out at SSRL beamline 11–3 (monochromatic X-ray, λ = 0.976 Å). The latter was collected as wide-angle X-ray scattering images with a LaB$_6$ crystal used for calibration. Rietveld refinements of XRD patterns were performed using the FullProf software. ICP measurements were performed using an inductively coupled plasma-optical emission spectrometry (ICP-OES) analyzer (Perkin Elmer OPTIMA 5300). Fluorine content in LTMOF was determined using fluorine ion-selective electrode (UX-27504–14) measurements. Sodium acetate

(Sigma-Aldrich) and total ionic strength adjustment buffer solutions (TISAB, Cole Parmer) were used to adjust the pH of the analyte.

X-ray spectroscopic imaging of the crystals was carried out using the transmission X-ray microscope installed at beamline 6−2c at the Stanford Synchrotron Radiation Lightsource (SSRL) of the SLAC National Accelerator Laboratory, which has a nominal spatial resolution of ≈30 nm. Details on the experimental configuration and the concept of the transmission X-ray microscopy (TXM)-based spectroscopic imaging method can be found elsewhere.[43−46] For the X-ray tomography measurement, X-ray transmissional images were measured at 6800 eV with the rotational angle scanned from −90 to 89° at an 1° interval. Reconstructed tomography was visualized by AVIZO software. For 2D XANES measurements, images at over 100 energy points were collected over the pre-edge and postedge region of Mn K-edge. While the energy step in the region away from the near edge is set to 15 eV to ensure coverage of a relatively large window needed for normalization, the energy step near the edge region was set to 1 eV to ensure sufficient energy resolution. Data analysis was performed using an in-house developed software package known as TXM-Wizard.[45−47]

The $L_{0.66}$TMOF sample for TEM study was prepared under the Thermo Scientific Helios NanoLab DualBeam microscope. Using focused ion beam (FIB), the lamellar TEM sample was lifted out from a $L_{0.66}$TMOF particle and then transferred onto the copper TEM grid for further thinning at a gradually reduced ion-beam voltage ranging from 30 to 2 kV. TEM imaging and diffraction studies were performed on a Titan 80−30 scanning/transmission electron microscope (S/TEM) operated at 300 kV. Time-of-flight (TOF) neutron powder diffraction experiments were performed using the POWGEN instrument at the Spallation Neutron Source (Oak Ridge National Laboratory). The data were collected at 300 K using the frame with a center wavelength of 0.8 Å and bandwidth of 1 Å. Rietveld refinement of the neutron diffraction data was performed using GSASII software package.[48]

4.3. Electrochemical Measurements. For composite electrode preparation, active materials were first ball-milled with acetylene carbon black (Denka, 20 wt %). The ball-milled mixture was then mixed with acetylene carbon black and a PVdF binder (Kynar 2801) in a 7:2:1 weight ratio in an NMP solvent. The mass ratio of the active material is 56 wt %. The slurry was casted onto an aluminum foil and dried overnight at 100 °C under vacuum. Cathode disks with an area of 1.6 cm^2 and a typical mass loading of 2−3 mg/cm^2 were used for cell testing. 2032-type coin cells were assembled in an argon-filled glovebox with Li foils (Alfa-Aesar) as counter and reference electrodes and Celgard 2400 membrane as separators. A solution of 1 M $LiPF_6$ in 1:1 (v/v) ethylene carbonate (EC)/diethylene carbonate (DEC) was used as the electrolyte carbonate (Novolyte Technologies Inc.). The cells were galvanostatically cycled using a VMP3 multichannel potentiostat/galvanostat. All electrochemical measurements were carried out at room temperature, and all cycling used a current density of 10 mA/g.

4.4. DFT Calculations. All first-principles calculations were performed in the Vienna Ab-Initio Simulation Package (VASP).[49−52] The projector augmented-wave (PAW) potentials[53,54] with the Perdew−Burke−Ernzerhof (PBE) generalized-gradient functional (GGA)[55] were used. All INCAR parameters used were benchmarked by the Materials Project and are documented in the MP Relax and MP Static sets in Python Materials Genomics (pymatgen).[56] All initial bulk structures were generated using a cluster expansion Monte Carlo method implemented by Ouyang et al.,[31] which is described elsewhere.[57] At a simulated temperature of 2573 °C, 300 000 Monte Carlo steps were used to equilibrate the structure and then 200 000 steps were used as a production run to generate structures. Forty-eight atom structures were generated for Li_2MnO_2F and 72 atom structures were generated for $LiMnO_2$.

To generate symmetric surfaces for this disordered material, initial bulk structures were first mirrored across the plane parallel to the (001) facet. The mirrored portion was then translated in the same plane for a half unit cell size to maintain proper FCC cation and anion ordering, resulting in the correct stoichiometry and symmetric surfaces from the point of view of the middle of the structure. The purpose of this operation is to make sure that the upper and bottom facets, both of which are exposed to vacuum, have the same atomic configuration. Bulk structure relaxations were then performed, and the relaxed bulk structures were used to create supercells of dimensions (1, 1, 2), and at least 15 Å of vacuum was added to create slabs. The total energy output from the relaxed bulk and slab calculations along with the dimensions of the surface of the slabs were used to calculate surface energies according to the following equation

$$\gamma = \frac{E_{slab} - N \times E_{bulk}}{2A}$$

where γ is surface energy, E_{slab} is the total energy output of the static slab calculation, N is the number of bulk layers in the supercell (2 for all calculations reported here), E_{bulk} is the total energy output of the bulk calculation, and A is the surface area of the slab.

ASSOCIATED CONTENT

Ⓢ Supporting Information

The Supporting Information is available free of charge at https://pubs.acs.org/doi/10.1021/acs.chemmater.1c02118.

XRD patterns and Rietveld refinement, SEM images and EDX elemental mapping, electrochemical analysis of LTMO and LTMOF cathodes, Williamson-Hall analysis, additional 2D XANES analysis of L_xTMO and L_xTMOF particles, schematics of slab cell construction and supporting figures of DFT analysis, supporting tables for refinement parameters of L_xTMO and L_xTMOF, and supplementary notes and references (PDF)

AUTHOR INFORMATION

Corresponding Authors

Yijin Liu − *Stanford Synchrotron Radiation Lightsource, SLAC National Accelerator Laboratory, Menlo Park, California 94025, United States*; Email: liuyijin@slac.stanford.edu

Guoying Chen − *Energy Storage and Distributed Resources Division, Lawrence Berkeley National Laboratory, Berkeley, California 94720, United States*; orcid.org/0000-0002-3218-2609; Email: gchen@lbl.gov

Authors

Dongchang Chen − *Energy Storage and Distributed Resources Division, Lawrence Berkeley National Laboratory, Berkeley, California 94720, United States*; orcid.org/0000-0002-2654-8176

Jin Zhang − *Stanford Synchrotron Radiation Lightsource, SLAC National Accelerator Laboratory, Menlo Park, California 94025, United States*

Zhisen Jiang − *Stanford Synchrotron Radiation Lightsource, SLAC National Accelerator Laboratory, Menlo Park, California 94025, United States*

Chenxi Wei − *Stanford Synchrotron Radiation Lightsource, SLAC National Accelerator Laboratory, Menlo Park, California 94025, United States*

Jordan Burns − *Energy Storage and Distributed Resources Division, Lawrence Berkeley National Laboratory, Berkeley, California 94720, United States; Department of Materials Science and Engineering, University of California, Berkeley, California 94720, United States*

Linze Li − *Environmental Molecular Sciences Laboratory, Pacific Northwest National Laboratory, Richland, Washington 99354, United States*; orcid.org/0000-0001-5362-8991

Chongmin Wang − *Environmental Molecular Sciences Laboratory, Pacific Northwest National Laboratory, Richland, Washington 99354, United States;* ⊙ orcid.org/0000-0003-3327-0958

Kristin Persson − *Molecular Foundry, Energy Sciences Area, Lawrence Berkeley National Laboratory, Berkeley, California 94720, United States; Department of Materials Science and Engineering, University of California, Berkeley, California 94720, United States;* ⊙ orcid.org/0000-0003-2495-5509

Complete contact information is available at:
https://pubs.acs.org/10.1021/acs.chemmater.1c02118

Author Contributions

Notes

The authors declare no competing financial interest.
The data that support the findings of this study are available from the corresponding authors upon reasonable request.

■ REFERENCES

(1) Whittingham, M. S. Lithium Batteries and Cathode Materials. *Chem. Rev.* **2004**, *104*, 4271−4302.

(2) Goodenough, J. B.; Kim, Y. Challenges for Rechargeable Li Batteries. *Chem. Mater.* **2010**, *22*, 587−603.

(3) Turcheniuk, K.; Bondarev, D.; Singhal, V.; Yushin, G. Ten years left to redesign lithium-ion batteries. *Nature* **2018**, *559*, 467−470.

(4) Yan, P.; Zheng, J.; Gu, M.; Xiao, J.; Zhang, J.-G.; Wang, C.-M. Intragranular cracking as a critical barrier for high-voltage usage of layer-structured cathode for lithium-ion batteries. *Nat. Commun.* **2017**, *8*, No. 14101.

(5) Yan, P.; Zheng, J.; Chen, T.; Luo, L.; Jiang, Y.; Wang, K.; Sui, M.; Zhang, J.-G.; Zhang, S.; Wang, C. Coupling of electrochemically triggered thermal and mechanical effects to aggravate failure in a layered cathode. *Nat. Commun.* **2018**, *9*, No. 2437.

(6) Mao, Y.; Wang, X.; Xia, S.; Zhang, K.; Wei, C.; Bak, S.; Shadike, Z.; Liu, X.; Yang, Y.; Xu, R.; Pianetta, P.; Ermon, S.; Stavitski, E.; Zhao, K.; Xu, Z.; Lin, F.; Yang, X.-Q.; Hu, E.; Liu, Y. High-Voltage Charging-Induced Strain, Heterogeneity, and Micro-Cracks in Secondary Particles of a Nickel-Rich Layered Cathode Material. *Adv. Funct. Mater.* **2019**, *29*, No. 1900247.

(7) Jiang, Z.; Li, J.; Yang, Y.; Mu, L.; Wei, C.; Yu, X.; Pianetta, P.; Zhao, K.; Cloetens, P.; Lin, F.; Liu, Y. Machine-learning-revealed statistics of the particle-carbon/binder detachment in lithium-ion battery cathodes. *Nat. Commun.* **2020**, *11*, No. 2310.

(8) Zhao, Y.; Stein, P.; Bai, Y.; Al-Siraj, M.; Yang, Y.; Xu, B.-X. A review on modeling of electro-chemo-mechanics in lithium-ion batteries. *J. Power Sources* **2019**, *413*, 259−283.

(9) Liu, P.; Xu, R.; Liu, Y.; Lin, F.; Zhao, K. Computational Modeling of Heterogeneity of Stress, Charge, and Cyclic Damage in Composite Electrodes of Li-Ion Batteries. *J. Electrochem.. Soc.* **2020**, *167*, No. 040527.

(10) Tippens, J.; Miers, J. C.; Afshar, A.; Lewis, J. A.; Cortes, F. J. Q.; Qiao, H.; Marchese, T. S.; Di Leo, C. V.; Saldana, C.; McDowell, M. T. Visualizing Chemomechanical Degradation of a Solid-State Battery Electrolyte. *ACS Energy Lett.* **2019**, *4*, 1475−1483.

(11) Huang, Z.; Boulatov, R. Chemomechanics: chemical kinetics for multiscale phenomena. *Chem. Soc. Rev.* **2011**, *40*, 2359−2384.

(12) Van Vliet, K. J. Chemomechanics of complex materials: challenges and opportunities in predictive kinetic timescales. *Sci. Model. Simul. SMNS* **2008**, *15*, 67.

(13) Luo, C.; Lei, Z.; Mao, Y.; Shi, X.; Zhang, W.; Yu, K. Chemomechanics in the Moisture-Induced Malleability of Polyimine-Based Covalent Adaptable Networks. *Macromolecules* **2018**, *51*, 9825−9838.

(14) Fu, C.; Venturi, V.; Kim, J.; Ahmad, Z.; Ells, A. W.; Viswanathan, V.; Helms, B. A. Universal chemomechanical design rules for solid-ion conductors to prevent dendrite formation in lithium metal batteries. *Nat. Mater.* **2020**, *19*, 758−766.

(15) Xu, Z.; Rahman, M. M.; Mu, L.; Liu, Y.; Lin, F. Chemomechanical behaviors of layered cathode materials in alkali metal ion batteries. *J. Mater. Chem. A* **2018**, *6*, 21859−21884.

(16) Mu, L.; Lin, R.; Xu, R.; Han, L.; Xia, S.; Sokaras, D.; Steiner, J. D.; Weng, T.-C.; Nordlund, D.; Doeff, M. M.; Liu, Y.; Zhao, K.; Xin, H. L.; Lin, F. Oxygen Release Induced Chemomechanical Breakdown of Layered Cathode Materials. *Nano Lett.* **2018**, *18*, 3241−3249.

(17) Xia, S.; Mu, L.; Xu, Z.; Wang, J.; Wei, C.; Liu, L.; Pianetta, P.; Zhao, K.; Yu, X.; Lin, F.; Liu, Y. Chemomechanical interplay of layered cathode materials undergoing fast charging in lithium batteries. *Nano Energy* **2018**, *53*, 753−762.

(18) Besli, M. M.; Xia, S.; Kuppan, S.; Huang, Y.; Metzger, M.; Shukla, A. K.; Schneider, G.; Hellstrom, S.; Christensen, J.; Doeff, M. M.; Liu, Y. Mesoscale Chemomechanical Interplay of the LiNi0.8Co0.15Al0.05O2 Cathode in Solid-State Polymer Batteries. *Chem. Mater.* **2019**, *31*, 491−501.

(19) Kim, H.; Kim, M. G.; Jeong, H. Y.; Nam, H.; Cho, J. A New Coating Method for Alleviating Surface Degradation of LiNi0.6-Co0.2Mn0.2O2 Cathode Material: Nanoscale Surface Treatment of Primary Particles. *Nano Lett.* **2015**, *15*, 2111−2119.

(20) Wang, H.; et al. TEM Study of Electrochemical Cycling-Induced Damage and Disorder in LiCoO[sub 2] Cathodes for Rechargeable Lithium Batteries. *J. Electrochem. Soc.* **1999**, *146*, 473−480.

(21) Wei, C.; Zhang, Y.; Lee, S.-J.; Mu, L.; Liu, J.; Wang, C.; Yang, Y.; Doeff, M.; Pianetta, P.; Nordlund, D.; Du, X.-W.; Tian, Y.; Zhao, K.; Lee, J.-S.; Lin, F.; Liu, Y. Thermally driven mesoscale chemomechanical interplay in Li0.5Ni0.6Mn0.2Co0.2O2 cathode materials. *J. Mater. Chem. A* **2018**, *6*, 23055−23061.

(22) Zhang, S. Chemomechanical modeling of lithiation-induced failure in high-volume-change electrode materials for lithium ion batteries. *npj Comput. Mater.* **2017**, *3*, No. 7.

(23) Lee, J.; Urban, A.; Li, X.; Su, D.; Hautier, G.; Ceder, G. Unlocking the Potential of Cation-Disordered Oxides for Rechargeable Lithium Batteries. *Science* **2014**, *343*, 519−522.

(24) Yabuuchi, N.; Takeuchi, M.; Nakayama, M.; Shiiba, H.; Ogawa, M.; Nakayama, K.; Ohta, T.; Endo, D.; Ozaki, T.; Inamasu, T.; Sato, K.; Komaba, S. High-capacity electrode materials for rechargeable lithium batteries: Li3NbO4-based system with cation-disordered rocksalt structure. *Proc. Natl. Acad. Sci. U.S.A.* **2015**, *112*, 7650−7655.

(25) Lee, J.; Kitchaev, D. A.; Kwon, D.-H.; Lee, C.-W.; Papp, J. K.; Liu, Y.-S.; Lun, Z.; Clément, R. J.; Shi, T.; McCloskey, B. D.; Guo, J.; Balasubramanian, M.; Ceder, G. Reversible Mn2+/Mn4+ double

redox in lithium-excess cathode materials. *Nature* **2018**, *556*, 185−190.

(26) Kan, W. H.; Chen, D.; Papp, J. K.; Shukla, A. K.; Huq, A.; Brown, C. M.; McCloskey, B. D.; Chen, G. Unravelling Solid-State Redox Chemistry in Li1.3Nb0.3Mn0.4O2 Single-Crystal Cathode Material. *Chem. Mater.* **2018**, *30*, 1655−1666.

(27) Fu, X.; Beatty, D. N.; Gaustad, G. G.; Ceder, G.; Roth, R.; Kirchain, R. E.; Bustamante, M.; Babbitt, C.; Olivetti, E. A. Perspectives on Cobalt Supply through 2030 in the Face of Changing Demand. *Environ. Sci. Technol.* **2020**, *54*, 2985−2993.

(28) Lun, Z.; Ouyang, B.; Kitchaev, D. A.; Clément, R. J.; Papp, J. K.; Balasubramanian, M.; Tian, Y.; Lei, T.; Shi, T.; McCloskey, B. D.; Lee, J.; Ceder, G. Improved Cycling Performance of Li-Excess Cation-Disordered Cathode Materials upon Fluorine Substitution. *Adv. Energy Mater.* **2019**, *9*, No. 1802959.

(29) Clément, R. J.; Lun, Z.; Ceder, G. Cation-disordered rocksalt transition metal oxides and oxyfluorides for high energy lithium-ion cathodes. *Energy Environ. Sci.* **2020**, *13*, 345−373.

(30) Lun, Z.; Ouyang, B.; Cai, Z.; Clément, R. J.; Kwon, D.-H.; Huang, J.; Papp, J. K.; Balasubramanian, M.; Tian, Y.; McCloskey, B. D.; Ji, H.; Kim, H.; Kitchaev, D. A.; Ceder, G. Design Principles for High-Capacity Mn-Based Cation-Disordered Rocksalt Cathodes. *Chem* **2020**, *6*, 153−168.

(31) Ouyang, B.; Artrith, N.; Lun, Z.; Jadidi, Z.; Kitchaev, D. A.; Ji, H.; Urban, A.; Ceder, G. Effect of Fluorination on Lithium Transport and Short-Range Order in Disordered-Rocksalt-Type Lithium-Ion Battery Cathodes. *Adv. Energy Mater.* **2020**, *10*, No. 1903240.

(32) House, R. A.; Jin, L. Y.; Maitra, U.; Tsuruta, K.; Somerville, J. W.; Forstermann, D. P.; Massel, F.; Duda, L.; Roberts, M. R.; Bruce, P. G. Lithium manganese oxyfluoride as a new cathode material exhibiting oxygen redox. *Energy Environ. Sci.* **2018**, *11*, 926−932.

(33) Chen, D.; Wu, J.; Papp, J. K.; McCloskey, B. D.; Yang, W.; Chen, G. Role of Redox-Inactive Transition-Metals in the Behavior of Cation-Disordered Rocksalt Cathodes. *Small* **2020**, *16*, No. 2000656.

(34) Chen, D.; Ahn, J.; Self, E.; Nanda, J.; Chen, G. Understanding cation-disordered rocksalt oxyfluoride cathodes. *J. Mater. Chem. A* **2021**, *9*, 7826−7837.

(35) Kuppan, S.; Xu, Y. H.; Liu, Y. J.; Chen, G. Y. Phase transformation mechanism in lithium manganese nickel oxide revealed by single-crystal hard X-ray microscopy. *Nat. Commun.* **2017**, *8*, No. 14309.

(36) Kan, W. H.; Deng, B.; Xu, Y.; Shukla, A. K.; Bo, T.; Zhang, S.; Liu, J.; Pianetta, P.; Wang, B.-T.; Liu, Y.; Chen, G. Understanding the Effect of Local Short-Range Ordering on Lithium Diffusion in Li1.3Nb0.3Mn0.4O2 Single-Crystal Cathode. *Chem* **2018**, *4*, 2108−2123.

(37) Kan, W. H.; Wei, C.; Chen, D.; Bo, T.; Wang, B. T.; Zhang, Y.; Tian, Y.; Lee, J. S.; Liu, Y.; Chen, G. Evolution of Local Structural Ordering and Chemical Distribution upon Delithiation of a Rock Salt−Structured Li1.3Ta0.3Mn0.4O2 Cathode. *Adv. Funct. Mater.* **2019**, *29*, No. 1808294.

(38) Yabuuchi, N.; Nakayama, M.; Takeuchi, M.; Komaba, S.; Hashimoto, Y.; Mukai, T.; Shiiba, H.; Sato, K.; Kobayashi, Y.; Nakao, A.; Yonemura, M.; Yamanaka, K.; Mitsuhara, K.; Ohta, T. Origin of stabilization and destabilization in solid-state redox reaction of oxide ions for lithium-ion batteries. *Nat. Commun.* **2016**, *7*, No. 13814.

(39) Kuppan, S.; Shukla, A. K.; Membreno, D.; Nordlund, D.; Chen, G. Revealing Anisotropic Spinel Formation on Pristine Li- and Mn-Rich Layered Oxide Surface and Its Impact on Cathode Performance. *Adv. Energy Mater.* **2017**, *7* (11), 1602010.

(40) Tian, C.; Xu, Y.; Nordlund, D.; Lin, F.; Liu, J.; Sun, Z.; Liu, Y.; Doeff, M. Charge Heterogeneity and Surface Chemistry in Polycrystalline Cathode Materials. *Joule* **2018**, *2*, 464−477.

(41) Alvarado, J.; Wei, C.; Nordlund, D.; Kroll, T.; Sokaras, D.; Tian, Y.; Liu, Y.; Doeff, M. M. Thermal stress-induced charge and structure heterogeneity in emerging cathode materials. *Mater. Today* **2020**, *35*, 87−98.

(42) Chen, D.; Kan, W. H.; Chen, G. Understanding Performance Degradation in Cation-Disordered Rock-Salt Oxide Cathodes. *Adv. Energy Mater.* **2019**, *9*, No. 1901255.

(43) Li, S.; Jiang, Z.; Han, J.; Xu, Z.; Wang, C.; Huang, H.; Yu, C.; Lee, S.-J.; Pianetta, P.; Ohldag, H.; Qiu, J.; Lee, J.-S.; Lin, F.; Zhao, K.; Liu, Y. Mutual modulation between surface chemistry and bulk microstructure within secondary particles of nickel-rich layered oxides. *Nat. Commun.* **2020**, *11* (1), 4433.

(44) Mao, Y.; Wang, X.; Xia, S.; Zhang, K.; Wei, C.; Bak, S.; Shadike, Z.; Liu, X.; Yang, Y.; Xu, R.; Pianetta, P.; Ermon, S.; Stavitski, E.; Zhao, K.; Xu, Z.; Lin, F.; Yang, X.-Q.; Hu, E.; Liu, Y. High-Voltage Charging-Induced Strain, Heterogeneity, and Micro-Cracks in Secondary Particles of a Nickel-Rich Layered Cathode Material. *Adv. Funct. Mater.* **2019**, *29* (18), 1900247.

(45) Liu, Y.; Meirer, F.; Wang, J.; Requena, G.; Williams, P.; Nelson, J.; Mehta, A.; Andrews, J. C.; Pianetta, P. 3D elemental sensitive imaging using transmission X-ray microscopy. *Anal. Bioanal. Chem.* **2012**, *404*, 1297−1301.

(46) Liu, Y.; Meirer, F.; Williams, P. A.; Wang, J.; Andrews, J. C.; Pianetta, P. TXM-Wizard: a program for advanced data collection and evaluation in full-field transmission X-ray microscopy. *J. Synchrotron Radiat.* **2012**, *19*, 281−287.

(47) Meirer, F.; Cabana, J.; Liu, Y.; Mehta, A.; Andrews, J. C.; Pianetta, P. Three-dimensional imaging of chemical phase transformations at the nanoscale with full-field transmission X-ray microscopy. *J. Synchrotron Radiat.* **2011**, *18*, 773−781.

(48) Toby, B. H.; Von Dreele, R. B. GSAS-II: the genesis of a modern open-source all purpose crystallography software package. *J. Appl. Crystallogr.* **2013**, *46*, 544−549.

(49) Kresse, G.; Hafner, J. Ab initio molecular dynamics for liquid metals. *Phys. Rev. B* **1993**, *47*, 558−561.

(50) Kresse, G.; Hafner, J. Ab initio molecular-dynamics simulation of the liquid-metal–amorphous-semiconductor transition in germanium. *Phys. Rev. B* **1994**, *49*, 14251−14269.

(51) Kresse, G.; Furthmüller, J. Efficiency of ab-initio total energy calculations for metals and semiconductors using a plane-wave basis set. *Comput. Mater. Sci.* **1996**, *6*, 15−50.

(52) Kresse, G.; Furthmüller, J. Efficient iterative schemes for ab initio total-energy calculations using a plane-wave basis set. *Phys. Rev. B* **1996**, *54*, 11169−11186.

(53) Blöchl, P. E. Projector augmented-wave method. *Phys. Rev. B* **1994**, *50*, 17953−17979.

(54) Kresse, G.; Joubert, D. From ultrasoft pseudopotentials to the projector augmented-wave method. *Phys. Rev. B* **1999**, *59*, 1758−1775.

(55) Perdew, J. P.; Burke, K.; Ernzerhof, M. Generalized Gradient Approximation Made Simple. *Phys. Rev. Lett.* **1996**, *77*, 3865−3868.

(56) Ong, S. P.; Richards, W. D.; Jain, A.; Hautier, G.; Kocher, M.; Cholia, S.; Gunter, D.; Chevrier, V. L.; Persson, K. A.; Ceder, G. Python Materials Genomics (pymatgen): A robust, open-source python library for materials analysis. *Comput. Mater. Sci.* **2013**, *68*, 314−319.

(57) Burns, J. P.; Ouyang, B.; Cheng, J.; Ceder, G.; Persson, K. A. Computational Determination of Equilibrium Particle Shape for Li2MnO2F.